Active truncation of slender marine structures: influence of the control system on fidelity

Thomas Sauder[a,c], Stefano Marelli[b], Kjell Larsen[d,a], Asgeir J. Sørensen[a]

[a] *Centre for Autonomous Marine Operations and Systems (NTNU AMOS), Department of Marine Technology, NTNU, 7491 Trondheim, Norway*
[b] *Chair of Risk, Safety and Uncertainty Quantification, Institute of Structural Engineering, ETH Zürich, Stefano-Franscini-Platz 5, CH-8093 Zürich, Switzerland*
[c] *SINTEF Ocean, P.O. Box 4762 Torgarden, 7465 Trondheim, Norway*
[d] *Statoil ASA, Arkitekt Ebbells veg 10, 7053 Ranheim, Norway*

Abstract

Performing hydrodynamic model testing of ultra-deep water floating systems at a reasonable scale is challenging, due to the limited space available in existing laboratories and to the large spatial extent of the slender marine structures that connect the floater to the seabed. In this paper, we consider a method based on real-time hybrid model testing, namely the *active truncation* of the slender marine structures: while their upper part is modelled physically in an ocean basin, their lower part is simulated by an adequate numerical model. The control system connecting the two substructures inevitably introduces artefacts, such as noise, biases and time delays, whose probabilistic description is assumed to be known. We investigate specifically how these artefacts influence the fidelity of the active truncation setup, that is its capability to reproduce correctly the dynamic behaviour of the system under study. We propose a systematic numerical method to rank the artefacts according to their influence on the fidelity of the test. The method is demonstrated on the active truncation of a taut polyester mooring line.

Keywords: ultra-deep water, active truncation, slender marine structures, real-time hybrid model testing, fidelity, control system, artefacts, sensitivity

1. Introduction

Floating structures used in the oil&gas, offshore wind or aquaculture industries require significant investments and must operate according to high safety and environmental standards. Therefore, the design of such structures is in general verified by means of hydrodynamic model testing prior to their construction. When performing such laboratory testing, the floating structure under study is constructed at reduced scale, and exposed to selected environmental conditions (wave, wind and current) that may be experienced during its design life. It is verified that the motions of the platform, the loads in the mooring and riser systems, or other quantities of interest (QoI) are acceptable under these conditions. The test campaign is in general also a final risk mitigation campaign, during which events not yet fully described by engineering numerical tools, such as green water and wave impact, could be detected and analyzed [1].

Floating structures are, however, installed at locations with increasingly large water depths. Oil exploitation takes nowadays place down to nearly 3000 m water depth [2], and deep-sea mining of minerals is considered in water depths reaching 6000 m [3]. Modelling such systems with a reasonably large scale factor in existing hydrodynamic laboratories is challenging, due to both the vertical extent of the mooring system, but also due to its horizontal footprint, that ranges from two to four times the water depth [4]. This

Email addresses: thomas.sauder@ntnu.no (Thomas Sauder), marelli@ibk.baug.ethz.ch (Stefano Marelli), klars@statoil.com (Kjell Larsen), asgeir.sorensen@ntnu.no (Asgeir J. Sørensen)

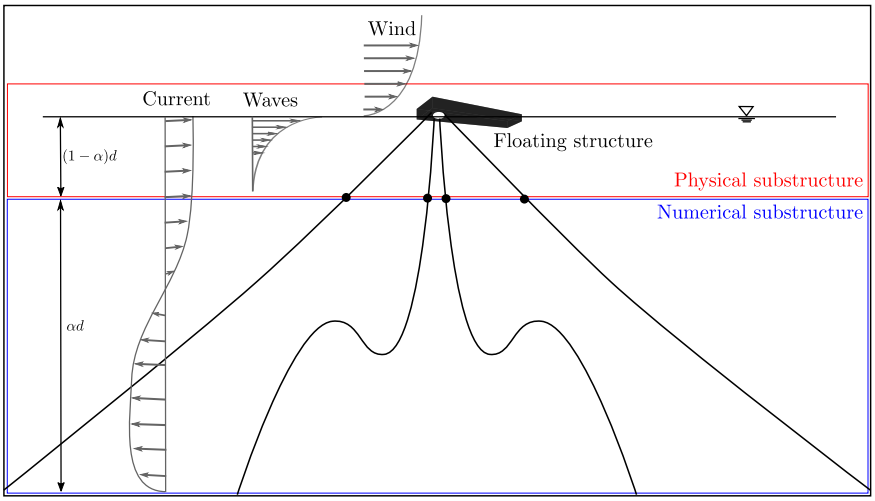

Figure 1: Model testing of an offshore structure with taut mooring and a flexible riser system in water depth d. Illustration of active truncation with truncation ratio $\alpha = 0.8$.

challenge has been identified two decades ago, and has been addressed in details in [5]. The state-of-the-art approach, up to now, consists in performing *passive truncation* of the slender marine structures, as described briefly in the following. In a first stage, a truncated version of the mooring/riser system is designed such that it is *statically equivalent* to the full-depth system, and fits in the ocean basin [6]. It should be emphasized that the *dynamic* properties of the truncated system, such as the level of drag-induced damping of the horizontal motions of the floater, are generally not representative of the full-depth system, except possibly on a narrow range of sea-states. Model testing is then performed using the truncated system, and the experimental results are used to calibrate a numerical hydrodynamic model *of the floater* connected to the truncated system. The truncated system is finally replaced by the full-depth one in the *numerical* analysis, and the QoI, such as extreme motions and mooring line tensions, are evaluated numerically. In spite of recent improvements in the truncation procedures, which have been reviewed for example in [7, 8], passive truncation still requires to calibrate a numerical model of the floater, which is time consuming and induces additional uncertainties. Furthermore, since the truncated system used in the model tests is only statically equivalent to the full-depth system, it can be argued that some highly nonlinear effects driven by the floater's dynamics (such as the occurrence of negative air gap or green water on deck) could remain undetected.

In the present paper, we consider an alternative solution denoted *active truncation*. It is based on the ReaTHM® testing[1] paradigm, already applied to solve issues related to model testing of floating wind turbines [9], and with applications beyond the field of marine technology [10, 11]. When performing active truncation, the floating structure and the upper part of the slender structure system are modelled *physically* in the ocean basin, while its lower part, which does not fit in the basin, is *simulated* on a computer. This is illustrated in Fig. 1. At the *truncation point*, the numerical and the physical *substructures* interact through a *control system*, including sensors and actuators. Therefore, active truncation intrinsically represents the full-scale system, and allows to obtain the QoI directly after the test, without the need for numerical extrapolation. Note that a strict pre-requisite to perform active truncation is the *validity of the numerical model describing the truncated portion of the slender marine structure.* In most cases, state-of-the-art programs based on the nonlinear Finite Element (FE) method can describe the low-frequency and wave-frequency dynamics of slender marine structures in a satisfactory manner, as for example illustrated in [12, Figure 2]. However, some phenomena, such as complex soil-structure interaction or Vortex-Induced Vibrations (VIV) can still not be simulated with a sufficiently high level of confidence, at least not in real-

[1]ReaTHM® testing stands for "Real-Time Hybrid Model testing", and is a registered trademark of SINTEF Ocean AS.

time. This means that, as of today, if these phenomena are very subject or play a significant role in the empirical study, ReaTHM testing can not be applied.

The uncertainties that affect purely empirical and numerical approaches have been extensively studied in the past [13, 14]. However, when performing active truncation (and ReaTHM testing in general), a new source of uncertainty should be considered, namely the one originating from an imperfect *coupling* between the substructures. Indeed, various types of *artefacts*, such as noise, biases and time delays, are inevitably introduced by the presence of the control system [15]. Such artefacts, could jeopardize the *fidelity* of the setup, in the sense that they could make the system's dynamical properties deviate significantly from those of the real system under study. In the worst case, this could happen without the operator of the test, or the final user of the empirical data, being aware of it. In this paper, we will neglect the uncertainties related to the physical and numerical substructures, to isolate and focus on those related to the control system.

This paper proposes a quantitative definition of fidelity, and presents a method to evaluate it for an active truncation setup. We then show how to systematically *identify the control system-induced artefacts that jeopardize the most the fidelity* (sensitivity study). This latter aspect is believed to be a significant scientific contribution, in addition to be of great operational relevance when such testing methods are to be applied in practice.

The paper is organized as follows. In Section 2, a general method for the analysis of fidelity is outlined, and we show how it can be applied to the active truncation of slender marine structures. This method requires the capability of simulating an active truncated setup, including artefacts, which is the object of Section 3. In Section 4, the method is demonstrated on the truncation of a taut polyester mooring line, which is a widely used component for the positioning of offshore structures in deep water.

2. Fidelity analysis and its application to active truncation

In this Section, we first introduce some concepts and terminology which will be used throughout the paper. We then define a quantitative measure of fidelity, and outline a general method to evaluate it and study its sensitivity to artefacts. We finally show how it can be applied to address the active truncation problem.

2.1. Background and terminology

The *real system* (Fig. 2a) is the subject of the study, whose performance under given load conditions should be documented. It is for example the marine system (floater, mooring and riser) represented in Figure 1. For analysis purposes, it is assumed that the real system can be fully represented by an *emulated system* (Fig. 2b). The emulated system consists of a numerical model capable of simulating the behaviour of the real system in a wide range of operational conditions, including extreme environmental conditions. For slender marine structures, the requirements and nature of this model strongly depends on the considered problem. Indeed, when VIV are neglected, top tensioned risers or taut polyester mooring lines in deep water can be satisfactorily simulated with linear time-domain (FE) methods, based on bar elements, and including nonlinear drag loads [16]. Other types of structures, such as flexible risers or steel catenary risers, require the modelling of geometric nonlinearities, bending stiffness, and possibly nonlinear material properties and soil-structure interaction [17].

Performing active truncation consists in splitting the slender marine structure into two *substructures* located on either side of a *truncation point* (Fig. 1). The *truncation ratio* α is defined as the ratio between the height of the water column occupied by the numerical substructure, and the total water depth d. At the truncation point, kinematic compatibility (equality of translational and rotational velocities) and dynamic equilibrium between the two substructures must be ensured at each instant. In more generic terms, the compatibility of *flow* and *effort* should be ensured at the interface between the substructure (Fig. 2c). To realize this in practice, a *control strategy* is chosen. As depicted in Fig. 2d, it can for instance be decided to *measure* the effort from the physical substructure (and prescribe it to the numerical substructure), and *prescribe* the flow (evaluated from the numerical substructure) to the physical substructure. In this way, the two substructures interact in real-time through a *control system* that includes sensors, actuators, as well as related software components such as force controllers and observers [15] (Fig. 2e).

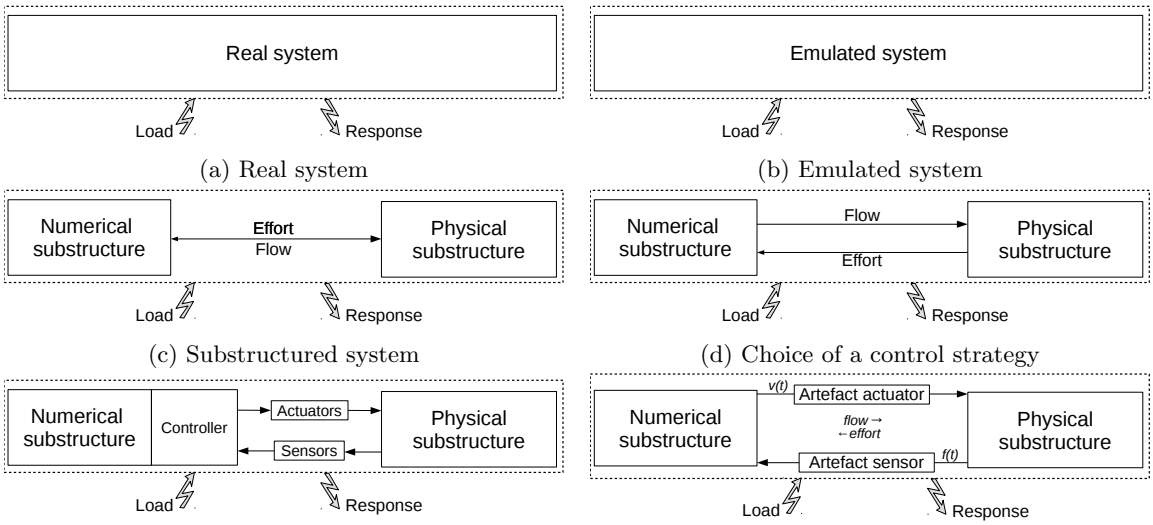

(a) Real system

(b) Emulated system

(c) Substructured system

(d) Choice of a control strategy

(e) Substructured system including control system.

(f) Modeling of the control system by artefacts.

Figure 2: The various steps, and associated terminology, in the design and analysis of real-time hybrid model testing in general, and active truncation in particular.

In reality, however, the control system inevitably introduces *artefacts*, such as measurement noise, time-delays due to communication, or imperfect actuation due to the actuators' own dynamics (Fig. 2f). The effects of some selected artefacts on a reference signal are illustrated in Fig. 3. Few authors have investigated the influence of such artefacts on the dynamics of substructured slender structures. The effect of interface time delays on substructured cables and beams have been studied analytically by [18] and [19], respectively. However, in both cases, the authors focus on the *stability* of the substructured system only. While stability is indeed a necessary condition for the execution of active truncation, it does not guarantee that the active truncation setup represents the real system in a satisfactory way. In a recent study, [20] compared the displacement field of a substructured beam to the one of the original beam (the emulated system) by using an L^2-based error measure. In this work, the beams were described by Bernoulli-Euler equations and subjected to harmonic loading. The artefacts introduced at the interface were constant amplitude and phase mismatches, which modelled imperfect actuators.

Studying fidelity of the active truncation problem with similar analytical approaches is challenging when marine structures are involved. The first and main reason is that such structures must in most cases be described by *purely numerical* methods, such as the nonlinear FE method, which are difficult to exploit in analytical derivations. Analytical formulations could admittedly be obtained by making strong assumptions on the behaviour of the structure, but this would lead to an emulated system that does not necessarily reflect the *real* system anymore, and would make the resulting analysis questionable. The second reason is related to the fact that a control system introduces not only one, but *several* types of artefacts *at the same time*. Suitable frameworks exist for studying the individual effect of each of these artefacts: stochastic differential equations, delayed differential equations, networked control systems theories allow for example to study the effect of noise, delays, and jitter, respectively. However, *combining* these frameworks leads to formulations that are intractable in practice. Also, making simplifying assumptions in this regard, by for example considering only one selected type of artefact, is questionable, since it is unclear *a priori* which artefact jeopardizes the fidelity, and which one can be neglected, if any. In the following subsection, we will outline a method to address these two issues.

2.2. Fidelity analysis method

Proposed definition of fidelity. The fidelity φ is calculated by comparing selected QoI, evaluated on the one hand from the emulated system (Fig. 2b), and on the other hand from the substructured system *including*

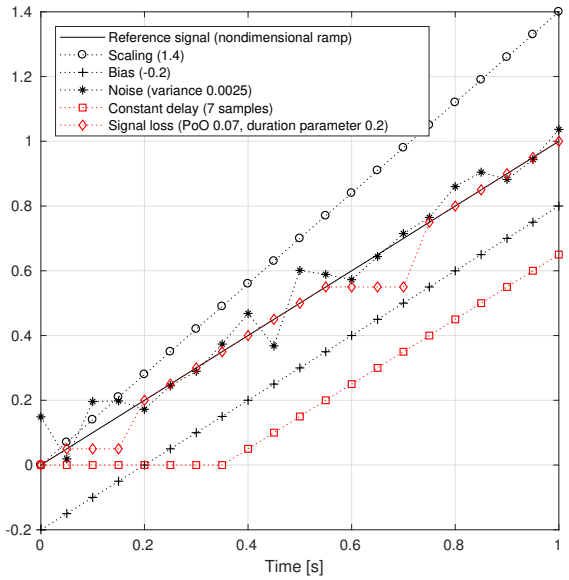

Figure 3: Various types of artefacts affecting a non-dimensional ramp signal, with their describing parameter in parentheses.

artefacts (Fig 2f), when these two systems are subjected to the *same* external excitation. The comparison function is chosen so that the value of φ tends to infinity when the QoI for the two systems are identical, and takes low values when the artefacts make the substructured and the emulated systems differ significantly. The selection of the external excitation, QoI, and comparison function is problem dependent, and we will propose a definition applicable to our active truncation problem in the next subsection.

Modelling of artefacts. As indicated in the legend of Fig. 3, each artefact is characterized by one or several parameters. For instance, white noise is described by its variance, and signal loss is described by both its probability of occurrence and its duration parameter. By gathering these parameters, the *heterogeneous set* of artefacts affecting the substructured system can be parametrized by a single M-components vector θ. In practice, the amount of noise or time delays present in an active truncation setup cannot be perfectly known until the setup has been realized. It is therefore considered that θ is the realization of a random vector Θ, with joint probability density function $f_\Theta(\theta)$. In the scope of this paper, the components of Θ are assumed to be statistically independent.

For a given realization θ of the artefacts' parameter, the fidelity $\varphi(\theta)$ can then be evaluated from *co-simulations* of the substructured system. The term co-simulation is used, since in the analysis, the physical and the numerical substructures are represented by *separate* numerical models, which are *coupled* at the truncation point in a dynamic simulation that includes the effect of the artefact. In Section 3, we will detail how this co-simulation is performed for slender marine structures.

Polynomial chaos expansions. Due to the random nature of the artefacts' parameter Θ, the fidelity $\varphi(\Theta)$ will also be a random variable, whose variance is assumed to be finite. It can then be approximated by the following (truncated) polynomial chaos expansion (PCE) [21]:

$$\hat{\varphi}(\Theta) := \sum_{\alpha \in \mathcal{A}} a_\alpha \psi_\alpha(\Theta) \tag{1}$$

where $\mathcal{A}$ a finite subset of $\mathbb{N}^M$, $(a_\alpha)_{\alpha\in\mathcal{A}}$ is a family of real numbers, $(\psi_\alpha)_{\alpha\in\mathbb{N}^M}$ a family of orthonormal polynomials with respect to the input variable Θ, i.e.

$$\mathrm{E}[\psi_\alpha(\Theta)\psi_\beta(\Theta)] = \int_{\mathcal{D}} \psi_\alpha(\theta)\psi_\beta(\theta) f_\Theta(\theta) d\theta := \delta_{\alpha\beta} \tag{2}$$

where $\delta_{\alpha\beta}$ is the Kronecker delta. Note that since the orthogonality condition in (2) depends on $f_\Theta(\theta)$, so does the chosen family of polynomials (ψ_α) in (1). We will demonstrate by an example in Section 4 how $\hat{\varphi}$ is determined in practice.

Uncertainty propagation. Thanks to the orthogonality property (2), estimates of $\mathrm{E}[\varphi(\Theta)]$ and of $\mathrm{Var}[\varphi(\Theta)]$ can be obtained from the a_α coefficients by:

$$\mathrm{E}[\hat{\varphi}(\Theta)] = a_0 \tag{3}$$

$$\mathrm{Var}[\hat{\varphi}(\Theta)] = \sum_{\alpha \in \mathcal{A}\setminus\{0\}} a_\alpha^2 \tag{4}$$

These estimates can then be related to a minimum admissible fidelity φ_{adm}, defined by the experimentalist, or the final user of the test results. Note that the value of φ_{adm}will depend on the exact definition of the fidelity, and will differ depending on the purpose of the test. For instance, if the active truncation tests aim at the final verification of a concept, one will aim at a high fidelity, and therefore a high value of φ_{adm}. If, on the contrary, they are related to a preliminary feasibility study, lower values of φ_{adm} could be accepted.

Sensitivity analysis. If $\mathrm{E}[\varphi(\Theta)]$ is deemed too low, or the uncertainty $\mathrm{Var}[\varphi(\Theta)]$ too large, the natural course of action is to determine which artefacts influence the most the variations of the fidelity. To do so, we will use the variance decomposition method (ANOVA), based on the Sobol' decomposition [22]. Under the assumption of finite variance, which we assume to be fulfilled for our physical problem, the following decomposition exists and is unique:

$$\varphi(\theta) = \varphi_0 + \sum_{i=1}^{M} \varphi_i(\theta_i) + \sum_{1\le i<j\le M} \varphi_{i,j}(\theta_i,\theta_j) + ... + \varphi_{1,2,...,M}(\theta_1,\theta_2,...,\theta_M) \tag{5}$$

where φ_0 is constant, and the integral of each summand over any of its independent variables is zero. In this setting, $\mathrm{Var}[\varphi(\Theta)] = \sum_{i=1}^{M} V_i + \sum_{1\le i<j\le M} V_{i,j} + ... + V_{1,2,...,M}$, where each term corresponds to the variance of the corresponding term in (5). Normalizing the above decomposition by $\mathrm{Var}[\varphi(\Theta)]$, the *Sobol' indices* are defined, which satisfy

$$\sum_{i=1}^{M} S_i + \sum_{1\le i<j\le M} S_{i,j} + ... + S_{1,2,...,M} = 1 \tag{6}$$

The S_i are called *first-order* Sobol' indices, $S_{i,j}$ *second order* Sobol' indices, etc... The *total* Sobol' indices $S_{T,i}$ are defined as the sum of all Sobol' indices involving the i^{th}parameter θ_i. By ranking the $S_{T,i}$, the θ_i having the greatest impact on the variations of the fidelity can be identified. Also, by comparing each $S_{T,i}$ to S_i, it is possible to evaluate whether parameter θ_i influences φ alone (in the case $S_i \approx S_{T,i}$), or jointly with other parameters of Θ.

The evaluation of Sobol' indices used to be computationally expensive, in the sense that numerous evaluations of $\varphi(\theta)$, and therefore numerous co-simulations of the substructured system, were required. However, it was recently shown in [23] how Sobol' indices could be computed analytically from the expansion (1). This result, associated with the significant advances on adaptive sparse PCEs [24], makes PCE a tool of choice for for uncertainty propagation and sensitivity analyses.

2.3. Fidelity indicators for the active truncation problem

Let us now show how this framework applies to our problem. We consider the active truncation of a mooring line connecting the floating structure to the sea bottom, as shown in Figure 1. Without loss of generality, we assume that the problem is two dimensional, and we define a direct x-z coordinate system, whose z axis is vertical and pointing upwards.

The fidelity will be evaluated by studying the response of the slender structure to a characteristic external load vector $\tau(t)$, with a duration T, in seconds. This load is meant to be representative, in terms of

amplitude, frequency content and direction, of a severe load that can be encountered during the testing of a truncated mooring line. The *dynamic* part of this load represents wave loads transferred from the floater to the slender structure, and is therefore applied to the top of the slender marine structure. It has two components. The first *low-frequency* component acts mainly axially, has an amplitude of 1MN, and a frequency content sweeping [0, 0.02] Hz. It mimics the effect of second-order difference-frequency wave loads. The *wave-frequency* component has an amplitude of 250kN, and a frequency content sweeping [0,0.2] Hz, and a direction with constant rate of change. This dynamic load comes in addition to the *static* top tension applied to the slender structure, and to the drag load associated to a shear current, whose velocity varies linearly throughout the water column for 0m/s at the seabed to 0.5m/s at the free surface. Time series of the top load can be seen in Fig. 5.

We will now focus on the definition of the fidelity indicator φ for the active truncation problem. In hydrodynamic model test campaigns, the focus is generally on the behaviour of the floater, and on extreme tensions in the slender marine structures, but not on their local deflection or curvature. The objective is therefore to make the interaction between the truncated slender marine structure, the (physical) floater and the (numerical) sea bottom reflect the corresponding interactions in a fully physical setup. In other words, *the exact behaviour of the slender structure throughout the water column is assumed of minor importance, as long as its interactions with the floater and the sea bottom are modelled properly.*

Based on this reasoning, two fidelity indicators are suggested. Let $V_{x,top}$ and $V_{z,top}$ be the components of the top velocity of the slender structure, and $F_{x,bottom}$ and $F_{z,bottom}$ the components of the force vector at its lower end. These values are calculated by co-simulation of the substructured system, that includes the artefacts parametrized by θ. Let $\bar{V}_{top}$ and $\bar{F}_{bottom}$ be their ideal counterparts, obtained by simulation of the emulated system. Then, the first indicator

$$\varphi_1(\theta) = -\frac{1}{2}\log_{10}\left(\frac{\int_0^T \left(V_{x,top}(t|\theta) - \bar{V}_{x,top}(t)\right)^2 dt}{\int_0^T \bar{V}_{x,top}(t)^2 dt} + \frac{\int_0^T \left(V_{z,top}(t|\theta) - \bar{V}_{z,top}(t)\right)^2 dt}{\int_0^T \bar{V}_{z,top}(t)^2 dt}\right) \tag{7}$$

quantifies how well the top end of the structure responds to the prescribed external load τ, and thus how well the substructured system manages to replicate the mechanical impedance of the slender structure. φ_1 is therefore important when motions of the floater are investigated. The second indicator

$$\varphi_2(\theta) = -\frac{1}{2}\log_{10}\left(\frac{\int_0^T \left(F_{x,bottom}(t|\theta) - \bar{F}_{x,bottom}(t)\right)^2 dt}{\int_0^T \bar{F}_{x,bottom}(t)^2 dt} + \frac{\int_0^T \left(F_{z,bottom}(t|\theta) - \bar{F}_{z,bottom}(t)\right)^2 dt}{\int_0^T \bar{F}_{z,bottom}(t)^2 dt}\right) \tag{8}$$

quantifies how well the external load is transferred to the sea bottom, and is then more relevant when the focus is on loads on e.g. anchors or blow-out preventers. If both aspects are important, φ_1 and φ_2 could easily be combined into a single indicator.

To summarize, in this Section, we have (1) suggested two possible expressions of the fidelity φ for the active truncation problem. (2) We discussed how φ could be jeopardized by heterogeneous and random artefacts, described by a random vector Θ. (3) We showed how $\mathrm{E}[\varphi(\Theta)]$ and $\mathrm{Var}[\varphi(\Theta)]$ could be evaluated (uncertainty propagation) from the PCE of φ, and (4) we introduced the Sobol' indices characterizing the sensitivity of φ to the various components of Θ. This analysis method will be demonstrated by a practical case study in Section 4. This case study requires the ability to co-simulate an active truncation setup including artefacts. This will be the object of the next section.

3. Co-simulation of slender marine structures including artefacts

The first part of this section describes a method to co-simulate the system presented in Fig. 2f, when the substructures are slender marine structure. As an example, the taut polyester mooring line, whose properties are given in Table 1, will be substructured, and a co-simulation will be performed, corresponding to a deterministic value of θ, to put in evidence the effect of selected artefacts on the dynamics of the system.

Table 1: Properties of the polyester mooring line used in the case studies.

Parameter	Unit	Value
Length	m	1934
Diameter	mm	264
Mass per unit length	kg/m	44.7
Young modulus	GPa	8.513
Submerged weight per unit length	N/m	93.2
Rayleigh damping coefficient α_2	s	$4.77.10^{-2}$
Top tension module	kN	2500
Top tension angle	^{o}	50
Normal added mass coefficient	-	1.0
Tangential added mass coefficient	-	0.0
Normal drag coefficient	-	1.6
Tangential drag coefficient	-	0.0

3.1. The `fixedFreeCableSegment` model

The FE method is used to simulate the slender marine structure. The analysis is two-dimensional, and the structure is represented by a bar element model (2 degrees of freedom per node) as shown in Fig. 4a. The boundary condition of the structure is *fixed-free* which means that the velocity of lower end of the structure, and the force on the upper end, are prescribed. Inertia, added-mass, drag and effective weight loads are included in a similar way as in [16]. The stiffness matrix has both an elastic and a geometric component. Since the geometric component strongly depends on the configuration of the structure, the static equilibrium is found by Newton-Raphson iterations.

The dynamic analysis is linear, in the sense that it uses the mass matrix M and the stiffness matrix K determined by the static analysis, throughout the time domain simulation. Nonlinearities due to drag loads are modelled exactly. These modelling choices are adequate to simulate structures with minimal changes of configuration, such as top tensioned risers or taut mooring lines in deep water, for which lateral deflections are about two orders of magnitude smaller than the structure's length. The structural damping matrix is of the form $C = \alpha_1 M + \alpha_2 K$ (Rayleigh damping) where α_1 is chosen to be null. In that case, the damping ratio associated to a vibration mode with circular frequency ω_i is $\lambda_i = \omega_i \alpha_2 / 2$. The model is implemented as a MATLAB® class named `fixedFreeCableSegment`. The verification of this class is presented in AppendixA. It is also shown how the eigenmodes of the taut polyester mooring differs from those of a string, due to the combined effects of elasticity, varying tension, and oblique configuration, which would be inconvenient to represent in a purely analytical model.

In the following, we will show how an active truncation setup can be modelled by coupling two such `fixedFreeCableSegment` objects.

3.2. Co-simulation without artefacts

The active truncation setup is represented in Fig. 4b. The water depth is d =1200 m, and the truncation ratio is α =0.8. The physical substructure (in red) and the numerical substructure (in blue), denoted `p` and `n`, respectively, are *each* modelled by a `fixedFreeCableStructure` object. The top velocity V_{top} in (7) will hence be evaluated from `p`, and the bottom force F_{bottom} in (8) from `n`. Focusing now on the truncation point, the selected boundary conditions in `fixedFreeCableSegment` are such that the bottom velocity of `p` and the top force acting on `n` can be prescribed. Their dual values, that is the bottom force on `p`, and the top velocity of `n`, can be evaluated by time integration. The dynamic equilibrium and kinematic compatibility at the truncation point is satisfied by the iterative procedure described in Algorithm 1.

There are three important parameters in this algorithm. The *synchronization time step* δt is the duration between two time instants at which equilibrium and compatibility at the truncation point are enforced. In practice, δt will be chosen equal to the minimum loop time of the control system orchestrating the active truncation. During the iterations (lines 6-14), ϵ_f and ϵ_v are force and velocity tolerances, below which dynamic equilibrium and kinematic compatibility at the truncation point are assumed to be achieved, respectively. These parameters influence both the results and the computational time of a co-simulation, in the same way as the number of elements n_{el}, so their value must be chosen carefully. To this end,

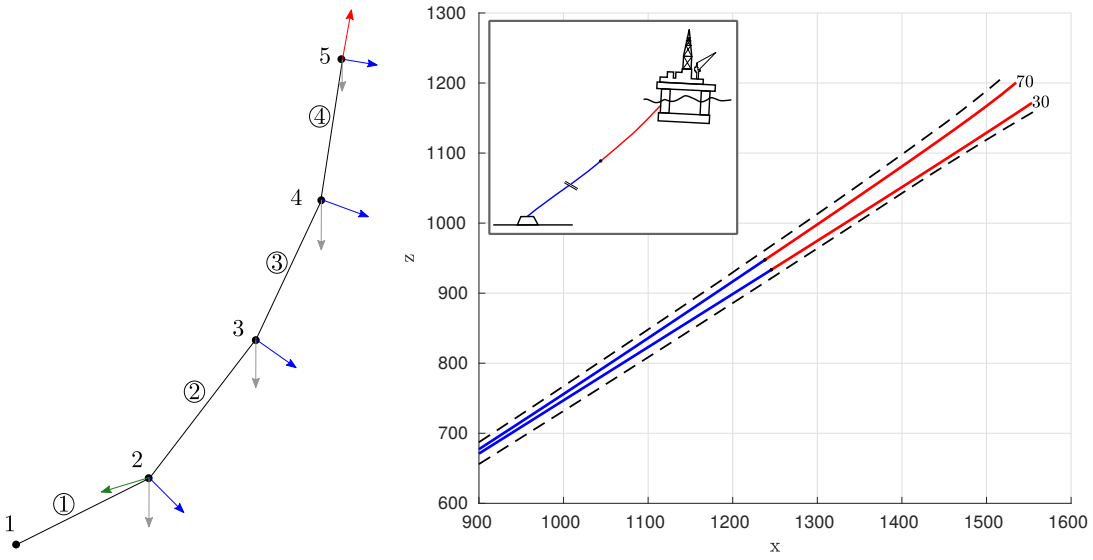

(a) Bar element model.

(b) Substructuring in the active truncation problem

Figure 4: Subfigure (a): bar element model as implemented in the `fixedFreeCableSegment` class. Element numbers are circled. Nodal forces are represented by arrows: effective weight force (grey), current forces (blue), prescribed external top force (red) and prescribed bottom displacement (green). Subfigure (b): overview of active truncation problem on the top left, with the physical substructure in red and the numerical substructure in blue. Main plot: snapshots of the upper part of the polyester line at $t = 30s$ and $t = 70s$, when subjected to the characteristic excitation τ. The dashed lines correspond to the envelope of the line's displacement during the analysis.

Algorithm 1 Co-simulation of two coupled `fixedFreeCableSegment` objects, denoted `n` and `p`.

for $t \in \{0, \delta t, ..., T - \delta t\}$ **do**
`v` ←top velocity of `n` at time instant t
`v_next` $\leftarrow \infty$
`f` ←bottom force of `p` at time instant t
`f_next` $\leftarrow \infty$
    while true **do**
Perform time-integration of `p` from t to $t + \delta t$ with varying external excitation and bottom velocity varying linearly to `v`
`f_next` ←bottom force of `p` at $t + \delta t$
Perform time-integration of `n` from t to $t + \delta t$ with varying external excitation and top force varying linearly to `f_next`
`v_next` ←top velocity of `n` at $t + \delta t$
        if $||$`v_next` $-$ `v`$||_\infty > \epsilon_v$ `OR` $||$`f_next` $-$ `f`$||_\infty > \epsilon_F$ **then**: `v` $\leftarrow$ `v_next` ; `f` $\leftarrow$ `f_next`
        else: Jump to next synchronization time step
        end if
    end while
end for

a convergence study is performed and reported in AppendixB. The selected values are n_{el}=80 elements, δt=10 ms, ϵ_v=10^{-6} m/s and ϵ_f=0.1 N.

We have outlined how a co-simulation could be performed that satisfies equilibrium and compatibility criteria at the truncation point. Performing the fidelity analysis described in Section 2 requires now artefacts to be introduced in this coupling, which will be the object of the next subsection.

3.3. Co-simulation including artefacts

An `artefact` class was developed, which allows simulating calibration errors (multiplicative errors), bias (additive errors), white noise, delay, zero-order hold and signal loss. The class has a `signalIn` method to get an input, a `signalOut` method to retrieve an output, and in the particular case when no artefact should affect the signal, it works simply as a First-In-First-Out (FIFO) queue. When artefacts are present, the input is modified before being returned. As an example, in Fig. 3, successive calls to `signalOut` were made on `artefact` objects with different properties, which received identical samples of the reference signal via the `signalIn` method.

As shown in Fig. 2f, two `artefacts` objects are needed, one acting on the effort (here, force) obtained from the experimental substructure, and the other one acting on the flow (here, velocity) obtained from the numerical substructure. Because they act on signals which are obtained from sensors, or used as reference to actuators, they will be denoted `aS` and `aA`, respectively. In this setting, performing a co-simulation that includes the effect of these artefacts requires only minor modifications to Alg. 1. (1) At line 8, `f_next` should be input to `aS.signalIn`, and the output of `aS.signalOut` should be used instead of `f_next` in line 9. (2) Similarly, `v_next` should be passed through `aA` after line 10 before being used. (3) At line 11, the convergence criterion should be evaluated on the values *affected by the artefacts*.

3.4. Example: effect of signal loss in active truncation

We will now illustrate the capabilities of this algorithm, and of the `artefact` and `fixedFreeCableSegment` classes with an example. We will consider a co-simulation in which *signal loss* affects *both the measured force and the applied velocity*. Signal loss may for example be due to sensor and communication issues, or to unfinished calculations in the numerical substructure [15]. It is parametrized by a probability of occurrence $\zeta_1 \in [0, 1)$ and a characteristic duration parameter $\zeta_2 > 0$. The duration D of the signal loss (during which the signal is "frozen" to the last received value) is modelled as a random variable distributed as $f_D(d) = e^{-\zeta_2 d}/\zeta_2$. With this model, longer signal loss durations are expected for smaller values of ζ_2. In the present case, ζ_1 is set to 1%, and ζ_2 to 0.1. So in this case, the artefacts can be parametrized by $M = 4$ components, and $\theta = (1\%, 0.1, 1\%, 0.1)^\top$.

The mooring line is subjected to the characteristic excitation τ described in Section 2. The results of the co-simulation are presented in Fig. 5. The dynamic excitation at the top node (first row) is identical for the emulated structure (black) and the physical substructure (red). This disturbance travels along the physical substructure (`p`), and reaches the truncation point where a force is measured (second row, red line). This force is possibly subjected to signal loss (`aS`) before being transferred, as a top force, to the numerical substructure (second row, blue line). The numerical substructure (`n`) responds to this top force (third row, blue line), and this response, which may also be affected by some signal loss (`aA`), is used to command the bottom velocity of the physical substructure (third row, red line). The effect of these signal loss on the QoI, which are the top velocity and the bottom force, are shown in the fourth and fifth rows, respectively. The fidelity is evaluated by comparing these signals to the ones obtained with the emulated system (black lines). By applying (7) and (8), it is found that $\varphi_1 = 1.30$ and $\varphi_2 = 1.99$.

The right column in Fig. 5 shows a selected time window during which signal losses happen on the measured force and on the applied velocity. On the second row, we can for instance observe that the signal of the force sensor freezes for about half a second shortly after $t = 174$ s, since the red and blue lines differ from each other. On the third row, it can be seen that the velocity command signal freezes twice, first at $t = 176$ s for half a second, then for about 300ms.

An important remark is that the substructure *from which the signal comes* has no direct information of the occurrence of a signal loss, but is anyway affected indirectly by the feedback it receives from the other

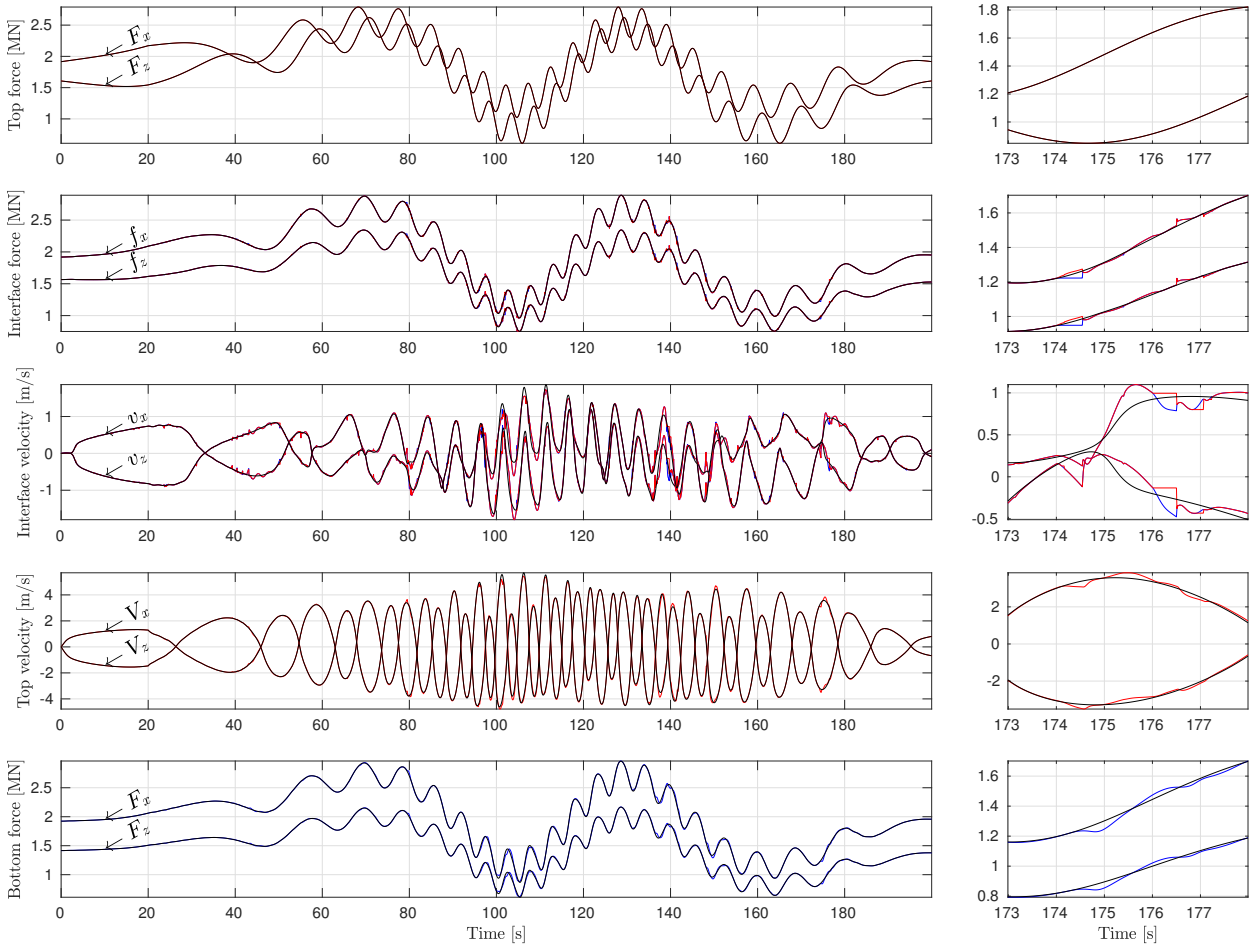

Figure 5: Active truncation setup subjected to the characteristic load τ. The red curves are obtained from the physical substructure, and the blue curves from the numerical substructure. The black curves represent the emulated system. Signal loss occurs at the force sensors level (as visible on the second row) and at the velocity actuation level (third row). The right column is a zoom on the time series at a location of interest.

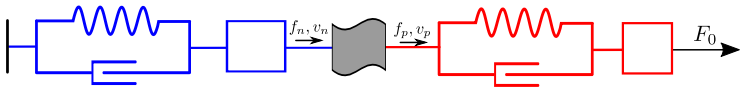

Figure 6: Stylized version of the active truncation problem, used to illustrate the effect of signal loss on the response of the substructures. The red mass-spring-damper (MSD) system represents the physical substructure, and the blue MSD system represents the numerical substructure. The flag-shaped box represents the truncation point, where signal loss occurs. F_0 represents the top excitation. f and v represent the force and velocity at the truncation point, respectively: f_n and v_n are seen from the numerical substructure, and f_p and v_p from the physical substructure.

substructure. Let us illustrate this by constructing a stylized version of our setup, represented in Fig. 6. We assume that signal loss occurs *on the force measurement only*, and that the velocity actuation is perfect, that is $v_p = v_n$ at all times, while $f_n \neq f_p$ when signal loss occurs. Starting from static equilibrium, when F_0 increases, all other variables f_p, f_n, v_p and v_n will increase. If signal loss occurs in the force measurement, f_n keeps a constant value (instead of increasing), and v_n will eventually decrease due to the stiffness and damping of the numerical substructure. Since v_n directly steers the actuator command, v_p will decrease immediately, causing the stretching of the physical substructure, and an in increase in f_p. When the signal on the force senors is recovered, f_n will jump to to the (larger) f_p value, causing a sudden increase of v_n, and thus v_p. This simplified example describes well the mechanism causing the significant decrease and increase of the velocity of the truncation point (on the physical substructure side) observed in Fig. 5 for $t \in [174, 176]$ s. This perturbation propagates according to the nonlinear dynamics of the slender structure, to the top and bottom ends of the line, and is clearly observed both on the top velocity and bottom force time series. It will thus affect both φ_1 and φ_2.

We have, in this Section, shown how the active truncation problem could be modelled, and with this last example, illustrated qualitatively the - possibly complex - interaction mechanisms resulting from e.g. signal losses at the truncation point. We will now extend the analysis to a larger set of *random* and *heterogeneous* artefacts, representing a more realistic case.

4. Fidelity analysis for a truncated taut mooring line

We will in this section show how the method presented in Section 2 can be applied to study the active truncation problem when multiple, heterogeneous and random artefacts are present. We consider the same polyester mooring line as in the previous example (see Table 1), installed in a water depth of $d = 1200$ m. Active truncation is performed with α =0.8. We assume that the model tests are performed at a scale $\lambda = 1/60$. This means that the depth of the ocean basin laboratory, where sensors and actuators are installed, is $(1 - \alpha)d\lambda = 4$ m. The two force components f_x and f_z at the truncation point are measured by two independent force sensors, and an actuator prescribes the velocity (v_x, v_z) of the truncation point. The mooring line is subjected to the characteristic load introduced in Section 2, and the fidelity indicators based on top velocity (φ_1) and bottom force (φ_2), defined in (7) and (8) are considered.

As shown in Figure 7 and Table 2, ten individual artefacts, described by $M = 12$ parameters, are assumed to affect the setup. The choice of including these artefacts, and neglecting others, is based on insight gained from the experimental work reported in [15], but note that the core method would apply also if other artefacts were selected. Each component of the force measurement is assumed to be contaminated by calibration error, bias, and noise. In the acquisition process, the force signals can be delayed, or lost, before entering the numerical substructure. Signal loss at the output of the numerical substructure models the fact that the calculations in the numerical substructure may not complete on time. An additional delay on the actuation side models computation and communication processes. The probabilistic description of these artefacts is summarized in the last column of Table 2. Since only estimates of upper bounds, lower bounds, mean values, or standard deviations of the θ_i parameters were available, the maximum entropy principle [25] was used to define $f_\Theta(\theta)$, which could be improved by dedicated surveys.

4.1. LHS sampling and uncertainty propagation

As outlined in Section 2, the first objective is to estimate $\mathrm{E}[\varphi(\Theta)]$, that is the expected fidelity for the active truncation setup, when it is affected by the set of artefacts described in Table 2. $\mathrm{Var}[\varphi(\Theta)]$ is also estimated, indicating how much the fidelity may vary due to the uncertainties on Θ. As explained in Section 2, this is done by establishing a PCE surrogate model of φ (in the following, φ may designate either φ_1 or φ_2), denoted $\hat{\varphi}$, whose structure allows to evaluate efficiently $\mathrm{E}[\varphi(\Theta)]$ and $\mathrm{Var}[\varphi(\Theta)]$. Such a surrogate model is a function of the twelve-dimensional variable θ, and must mimic the behaviour of φ over its whole domain of definition. To establish $\hat{\varphi}$, $\varphi(\theta)$ must therefore be evaluated for a *space-filling* set of samples of Θ denoted $\mathcal{E}$. This set is generated with the Latin Hypercube Sampling method (LHS), and φ is evaluated by co-simulation, as explained in Section 3, for each sample in $\mathcal{E}$. In Figure 8, the markers show 208 points

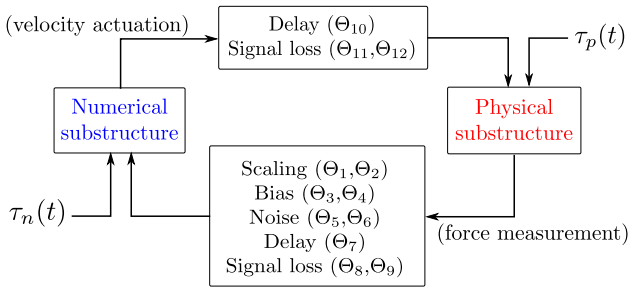

Figure 7: Block diagram of the active truncation setup, modelled artefacts, and their describing parameters. τ_n represents the current loads acting on the numerical substructure, and τ_p represents the current loads and varying wave-induced loads acting on the physical substructure.

Table 2: Description of the artefacts affecting the setup, including their probabilistic description. $\mathcal{U}(a,b)$ refers to the uniform distribution with support $[a,b]$. $\mathcal{N}(\mu,\sigma)$ refers to the normal distribution with mean μ and variance σ^2. Here λ=1/60 and δt=10 ms.

Type of artefact	Affected signal	Describing parameter(s)	Unit	Probabilistic description
Calibration error	f_x	Θ_1 (scaling factor)	-	$\mathcal{N}(1, 0.015)$
Calibration error	f_z	Θ_2 (scaling factor)	-	$\mathcal{N}(1, 0.015)$
Bias	f_x	Θ_3 (bias value)	N	$\mathcal{N}(0, 0.05\lambda^{-3})$
Bias	f_z	Θ_4 (bias value)	N	$\mathcal{N}(0, 0.05\lambda^{-3})$
Noise	f_x	Θ_5 (noise variance)	N^2	$\mathcal{U}((0.025\lambda^{-3})^2, (0.05\lambda^{-3})^2)$
Noise	f_z	Θ_6 (noise variance)	N^2	$\mathcal{U}((0.025\lambda^{-3})^2, (0.05\lambda^{-3})^2)$
Delay	f_x,f_z	Θ_7 (duration)	s	$\mathcal{U}(0, 5\delta t)$
Signal loss	f_x,f_z	Θ_8 (probability of occurrence) Θ_9 (duration parameter)	- s^{-1}	$\mathcal{U}(1\%, 10\%)$ $\mathcal{U}(0.1, 0.5)$
Delay	v_x,v_z	Θ_{10} (duration)	s	$\mathcal{U}(0, 5\delta t)$
Signal loss	v_x,v_z	Θ_{11} (probability of occurrence) Θ_{12} (duration parameter)	- s^{-1}	$\mathcal{U}(1\%, 10\%)$ $\mathcal{U}(0.1, 0.5)$

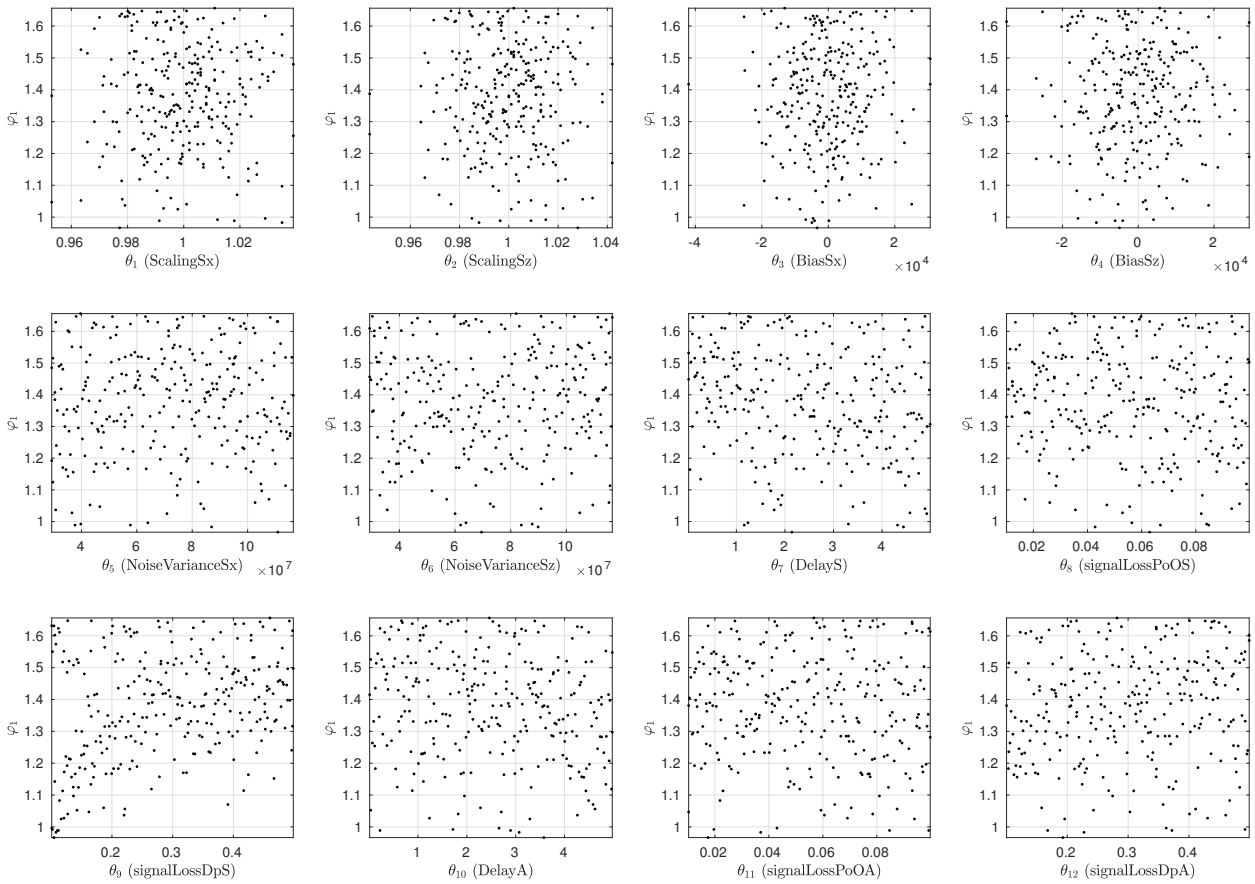

Figure 8: Scatter diagrams showing the value of φ_1 (fidelity indicator based on the top velocity of the line), as a function of the twelve parameters describing the artefacts. The dots correspond to 208 samples of Θ obtained by Latin Hypercube Sampling (set denoted $\mathcal{E}$ in the text).

generated by LHS in the twelve-dimensional space, with the associated value of φ_1 plotted against each component of θ. Note that these co-simulations are independent from each other and can therefore be performed in parallel. Also, nested LHS can be used [26], to sequentially add samples to $\mathcal{E}$, while ensuring that the updated set $\mathcal{E}$ contain samples still distributed according to $f_\Theta(\theta)$. The distribution of φ can be estimated from $\mathcal{E}$ (see Figure 9), and in Figure 10, the realization of Θ leading to the median value of φ_1 is shown for illustration.

Based on this initial set $\mathcal{E}$ and on the associated values of φ, the PCE model $\hat{\varphi}$ in (1) is established by using a degree-adaptive sparse PCE, based on least-angle regression (LARS, [24]), implemented in the UQLab software [27, 28]. These two references may be consulted by the interested reader for more details on the theoretical and practical aspects of PCE identification. The values of $\mathrm{E}[\varphi(\Theta)]$ and $\mathrm{Var}[\varphi(\Theta)]$ can then be evaluated from (3) and (4):

$$E[\hat{\varphi}_1(\Theta)] = 1.32 \text{ and } \mathrm{Var}[\hat{\varphi}_1(\Theta)] = 0.13^2$$

$$E[\hat{\varphi}_2(\Theta)] = 1.77 \text{ and } \mathrm{Var}[\hat{\varphi}_2(\Theta)] = 0.17^2$$

This means that the active truncation scenario selected in Figure 10, where φ_1=1.33 and φ_2=1.62, corresponds to an *average fidelity* for the top velocity of the slender structure (when compared to $E[\varphi_1]$), and to a *quite poor fidelity* for the bottom force (when compared to $E[\varphi_2]$).

As this will be used in the following, let us mention that we can quantify how well $\hat{\varphi}$ reproduces the behaviour of φ by using the Leave-One-Out cross validation (LOO) error. It is established as follows. *For*

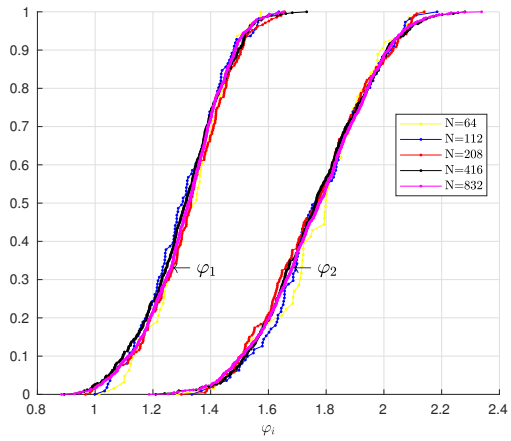

Figure 9: Cumulative distribution functions of φ_1 and φ_2 obtained from sets $\mathcal{E}$ of different sizes.

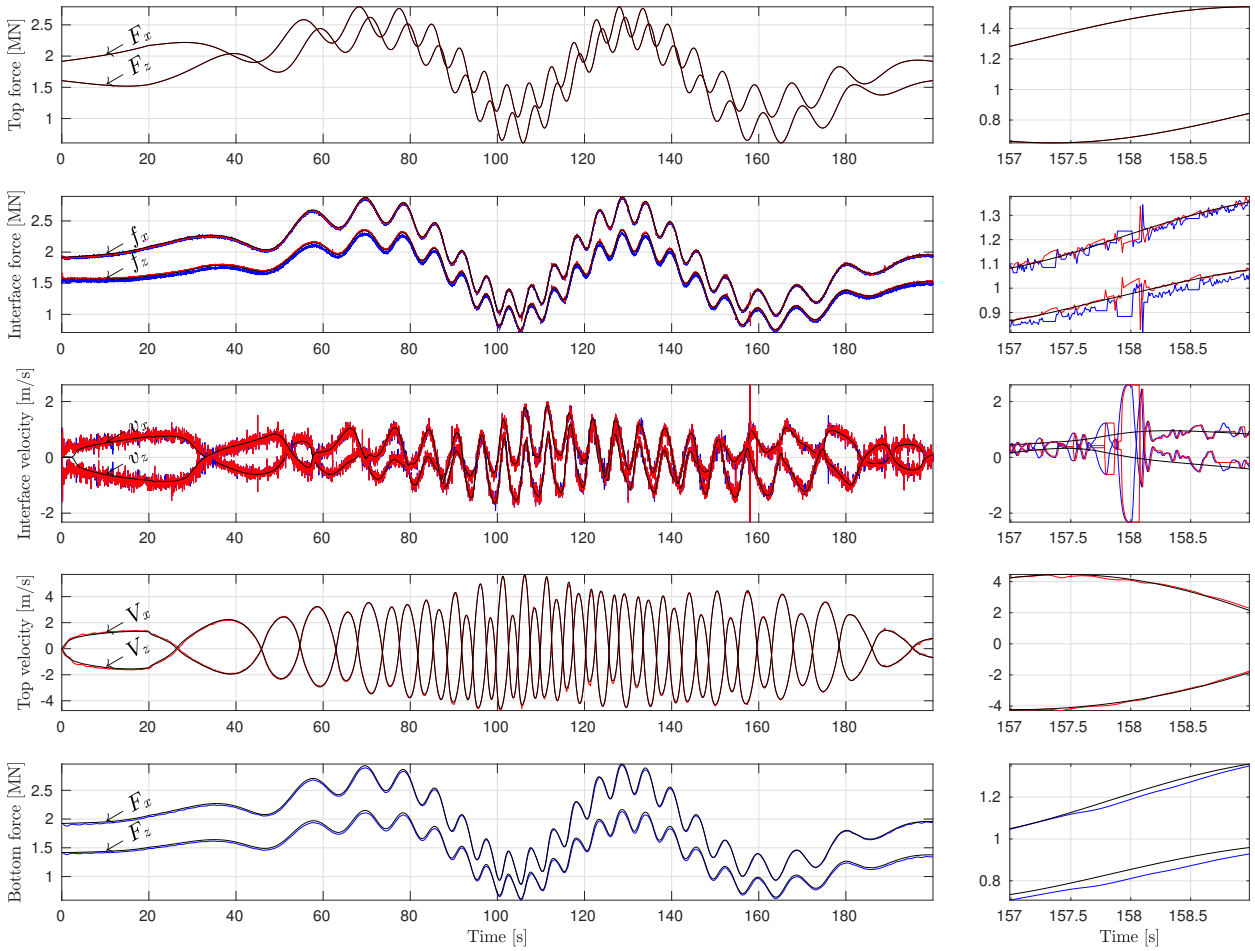

Figure 10: Co-simulation of active truncation with a set of the artefacts leading to the *median* value of φ_1. For this realization, the measurement of f_x (resp. f_z) is affected by a -0.3% (resp. -3%) calibration error, a -0.012 N (resp. 0.28 N) bias, and noise with a standard deviation of 0.040 N (resp. 0.037N), in model scale. The force measurement is delayed by 2.6ms, and has a probability of signal loss of 7.5%, with a duration parameter of 0.47, which corresponds to frequent and short periods of signal loss. On the actuation side, the delay is 1.3ms, and the probability of occurrence and duration parameter of signal loss are 6.8 % and 0.17, respectively. The resulting fidelity indicators are φ_1=1.33 and φ_2=1.62.

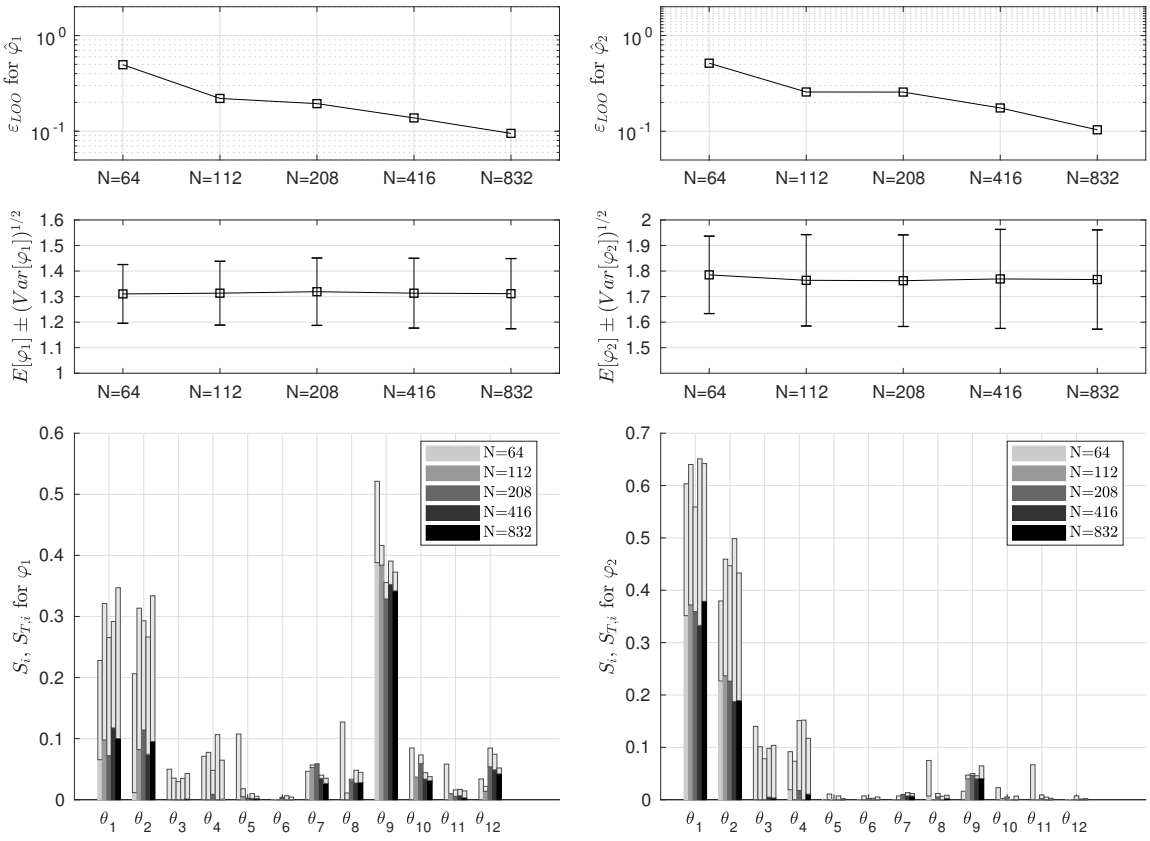

(a) Results for φ_1 (b) Results for φ_2

Figure 11: Upper plot: normalized Leave-One-Out cross-validation error for the PCE metamodel of φ_i. Middle plot: expected value and variance of φ_i estimated from initial empirical designs of five different sizes. Lower plot: first-order Sobol' indices of φ_i estimated from these initial experimental designs. The corresponding *total* Sobol' index of each θ_i is plotted in grey in the background.

each sample $\theta^* \in \mathcal{E}$, a PCE model is established based on the set $\mathcal{E} \setminus \theta^*$, and the values of $\varphi(\theta^*)$ and $\hat{\varphi}(\theta^*)$ are compared. Even if this means that, in principle, as many PCE models should be established as elements in $\mathcal{E}$, the LOO error can under some circumstances be estimated directly from the single PCE model established from the whole set $\mathcal{E}$ [28]. The LOO error (normalized by the variance of $\hat{\varphi}$) is usually deemed satisfactory for uncertainty propagation and sensitivity analyses, when it does not exceed 10^{-1} [29]. This will be commented on later on.

4.2. Sensitivity analysis

In some cases, visual inspection of scatter diagrams such as Figure 8, allows one to determine directly which artefact component(s) affects the most the fidelity. This becomes however more difficult for increasing values of M (the dimension of θ), and particular for the present case with $M = 12$. As introduced in Section 2, Sobol' sensitivity indices can instead be used, which are directly deduced from $\hat{\varphi}$. Before looking at the Sobol' indices, let us recall that the *absolute* values of the total Sobol' indices $S_{T,i}$ are of secondary importance: the $S_{T,i}$ should be *compared to each other* to identify the most influencing artefacts' parameters. Furthermore, $S_{T,i}$ can be compared to the first order Sobol' index S_i, to understand whether the artefact parameter θ_i influences the variance of φ alone, or in an interaction with another parameter θ_j, or several others.

With these interpretation keys in mind, let us consider the bottom plots in Figure 11, showing the $S_{T,i}$ and S_i, estimated from various sizes (or cardinality) $card(\mathcal{E})$ of $\mathcal{E}$. It is seen that for the present problem,

reliable insight into the main mechanisms of sensitivity can be obtained for $card(\mathcal{E})$=208. If $card(\mathcal{E})$=416, finer conclusions can be made regarding the sensitivity to less important parameters, which do not change when $card(\mathcal{E})$=832. For both $card(\mathcal{E})$=208 and 416, the estimated statistical moments are within 1% of the value obtained with for $card(\mathcal{E})$=832 samples. Note that the recommended values of the LOO error in [29] are rather conservative for the present situation, since good convergence of the statistical moments and meaningful sensitivity information are obtained, in spite of an LOO error exceeding 0.1.

Let us first outline the main conclusions that can be drawn from the total Sobol' indices $S_{T,i}$, represented by grey bars in Figure 11b (consider for example $card(\mathcal{E})$=416). The fidelity indicator based on the *top velocity* response, φ_1, is very sensitive to θ_9 (the duration of the signal loss on the force signal) and to the calibration errors of the f_x and f_z measurement (θ_1 and θ_2). φ_1 is much less sensitive to the other θ_i, and clearly insensitive to noise (described by θ_5 and θ_6). Focusing now on the *bottom force*, we see that φ_2 is mostly sensitive to θ_1, then θ_2 (calibration errors), and then to a much less extent to the biases θ_3 and θ_4, which have both comparable total Sobol' indices. φ_2 is slightly sensitive to θ_9, the duration parameter for signal loss on the force measurement, and insensitive to the other θ_i parameters. We will now relate these results, obtained by a systematic approach, to their physical causes.

The effect of white noise. It is clear from Figure 10 that the noise affecting force measurements (parametrized by θ_5 and θ_6) induces a significant velocity response at the truncation point. This response is however filtered mechanically by drag and, to a less extent, structural damping, before reaching the top and bottom of the mooring line. Therefore noise does not significantly affect the fidelity indicators φ_1 and φ_2. The fact that the $S_{T,i}$ associated to this artefact are negligible, means that the corresponding parameters θ_5 and θ_6 (noise variances) could have been set to deterministic values (here, zero), without affecting the variance of φ.

Signal loss. A natural question when looking at Fig. 11a, is why the top velocity (or φ_1) is more sensitive to signal loss, when it acts on the force sensor (duration parameter θ_9) rather than when it acts on the velocity actuation (parameter θ_{12}). Indeed, the force sensors feeds the numerical substructure, while the actuator controls the bottom part of the physical substructure, whose response *directly* enters in the definition (7) of φ_1. The reason is the following. When signal loss on the velocity command happens, the velocity of the truncation point keeps a *constant* value. On the other hand, signal loss on the force sensor may cause *large variations* of the truncation point's velocity, due to the interaction with the numerical substructure that was commented in detail in Section 3 and seen in Figure 5. Both the *amplitude* of these perturbations and their *duration* increase when the signal loss characteristic duration increases, which enhances their propagation to the top of the mooring line.

Effect of the anisotropic properties of the mooring. The fact that φ_2 is more sensitive to θ_1 (calibration error for f_x measurement) than to its counterpart θ_2 (acting on f_z) can be explained as follows. Transverse motions of the mooring line are subjected to drag damping forces, while axial motions are only damped by structural damping, which means that, with the present choice of α_2 and the present frequency range of motions, transverse motions will be subjected to a significantly higher level of damping than axial motions. Consequently, an axial dynamic force error will be less damped than its transverse counterpart. Since the mooring line forms an angle of $\gamma = 39.2\ ^o$ with respect to the x-axis at the truncation point, the axial forces have an x-component larger than their $z-$ component, and a calibration error on f_x (parametrized by θ_1) will play a greater role for φ_2 than a calibration error on f_z (parametrized by θ_2).

Also, as explained earlier, Total Sobol' indices and first-order indices differ when there is an interaction between two (or more) θ_i. The nature of this interaction can be determined by considering higher-order Sobol' indices (not shown here). Note that in principle, a finer PCE model (with lower LOO error) would be needed to obtain accurate estimates of the higher-order Sobol' indices, so only trends will be commented here. We found for example that the interaction between θ_1 and θ_2 explains $\approx 20\%$ of the variance of φ_1, and $\approx 15\%$ of the variance of φ_2. This is due to the fact that if θ_1 and θ_2 differ significantly from each other, the *direction* of the force at the truncation point will be affected. Since the stiffness and damping properties of the line are not isotropic, as explained earlier, this change in *direction* will have a significant effect on the fidelity.

Effect of the bias. From Figure 11, we see that biases have a significant influence on φ_1 and φ_2 (total Sobol indices), and that this influence is due to interactions ($S_5 \ll S_{T,5}$ and $S_6 \ll S_{T,6}$ in both cases). Here, the mechanisms in play are slightly different for φ_1 and φ_2.

By again studying higher-order Sobol indices, it can be shown that the interaction between θ_1 and θ_3 (resp. θ_2 and θ_4) explains $\approx 10\%$ of the variance of φ_2. This interaction is induced by the *pretension* at the truncation point, denoted T_0^*. Indeed, for example, when a scaling error θ_1 affects f_x only, it is equivalent to a bias of $(\theta_1 - 1)T_0^* \cos\gamma$ being added to θ_3, and transferred to the anchor point. Coupling terms between θ_1 and θ_3 will therefore be generated in the Sobol' decomposition (5) of φ_2, due to the logarithm in (8).

Biases should, in principle have little influence on φ_1, since constant force will simply lead to a constant offset, and not change the (linear) dynamical properties of our substructures. However, about $\approx 10\%$ of the variance of φ_1 is due to one-to-one interactions between θ_1, θ_2, θ_3, and θ_4. This is due to the following effect. In the horizontal direction, for $t < 0$, the component of the pretension is $T_0^* \cos\gamma$ at the truncation point. For $t \geq 0$, it suddenly changes to $\theta_3 + (\theta_1 - 1)T_0^* \cos\gamma$, when artefacts are applied to the force signal. This impulsive load causes a transient response, visible in Figure 10, which has a minor, but noticeable, influence on φ_1.

5. Conclusion

In the present paper, we considered active truncation as an alternative technique to perform model testing of ultra-deep water floating systems in existing ocean laboratories. We assessed the performance of an active truncation setup through its associated fidelity. We showed how the fidelity could be jeopardized by multiple, heterogeneous and random artefacts, originating from the control system (including sensors, actuators and controllers) that connects the numerical and physical parts of the setup. We outlined a method to evaluate the expected fidelity of the setup, and its variability due to the uncertainties on the artefacts. Finally, a *systematic* analysis method based on Sobol' indices allowed us to determine the sensitivity of the fidelity to each of the involved artefacts. This latter result provides valuable and objective indications to improve fidelity in an operational context. Using the polynomial chaos expansions of the fidelity made this sensitivity analysis possible at a reasonable computational cost.

A case study addressing a taut polyester mooring line allowed to gain insight in the complex mechanisms taking place in active truncation, combining the dynamics of the slender structures and the imperfect coupling at the truncation point. A total of ten artefacts were included in the analysis, and the importance of calibration errors and signal loss at the force sensors level was put in evidence. It must be emphasized that, since the fidelity is a nonlinear function of the artefacts parameters, these conclusions are valid for the present system and set of artefacts only.

The present method is currently extended to a complete framework, which also allows to (1) determine the feasibility of an active truncation test, by evaluating its probability of failure due to too low fidelity, and (2) determine the corresponding admissible bounds on the artefact parameters.

Acknowledgment

This work was supported by the Research Council of Norway through the Centres of Excellence funding scheme, Project number 223254 - AMOS, and through the project 254845/O80 “Real-Time Hybrid Model Testing for Extreme Marine Environments”.

References

[1] C. Pakozdi, A. Östman, B. C. Abrahamsen, O. D. Økland, T. M. Vestbøstad, G. Lian, C. T. Stansberg, New Combined CFD and Model Testing Technique for Identification of Wave Impact Loads on a Semisubmersible, in: ASME 2017 36th International Conference on Ocean, Offshore and Arctic Engineering, American Society of Mechanical Engineers, 2017, pp. V001T01A089–V001T01A089.

[2] S. Bowers, Shell begins production at world's deepest underwater oilfield, The Guardian, September 11th, 2016.

[3] R. Sharma (Ed.), Deep-Sea Mining, Springer International Publishing, Cham, 2017. doi:10.1007/978-3-319-52557-0.

[4] M. Randolph, S. Gouvernec, Offshore Geotechnical Engineering, CRC PRESS, S.l., 2017, oCLC: 991684040.
[5] C. T. Stansberg, H. Ormberg, O. Oritsland, Challenges in Deep Water Experiments: Hybrid Approach, Journal of Offshore Mechanics and Arctic Engineering 124 (2) (2002) 90. doi:10.1115/1.1464129.
[6] I. Fylling, C. T. Stansberg, Model Testing of Deepwater Floating Production Systems: Strategy for Truncation of Moorings and Risers, in: DOT Brazil, 2005.
[7] T. Sauder, A. J. Sørensen, K. Larsen, Real-Time Hybrid Model Testing of a Top Tensioned Riser: A Numerical Case Study On Interface Time-Delay and Truncation Ratio., in: ASME 2017 36th International Conference on Ocean, Offshore and Arctic Engineering, Trondheim, Norway, 2017.
[8] Y. Cao, G. Tahchiev, A Study on an Active Hybrid Decomposed Mooring System for Model Testing in Ocean Basin for Offshore Platforms, in: ASME 2013 32nd International Conference on Ocean, Offshore and Arctic Engineering, American Society of Mechanical Engineers, 2013.
[9] T. Sauder, V. Chabaud, M. Thys, E. E. Bachynski, L. O. Sæther, Real-time Hybrid Model Testing of a Braceless Semi-submersible Wind turbine. Part I: The Hybrid Approach, in: ASME 2016 35th International Conference on Ocean, Offshore and Arctic Engineering, No OMAE2016-54435, 2016.
[10] C. S. Edrington, M. Steurer, J. Langston, T. El-Mezyani, K. Schoder, Role of Power Hardware in the Loop in Modeling and Simulation for Experimentation in Power and Energy Systems, Proceedings of the IEEE 103 (12) (2015) 2401–2409. doi:10.1109/JPROC.2015.2460676.
[11] D. McCrum, M. Williams, An overview of seismic hybrid testing of engineering structures, Engineering Structures 118 (2016) 240–261. doi:10.1016/j.engstruct.2016.03.039.
[12] V. Aksnes, P. A. Berthelsen, N. M. M. D. Da Fonseca, On the need for calibration of numerical models of large floating units against experimental data, in: The Twenty-Fifth International Ocean and Polar Engineering Conference, International Society of Offshore and Polar Engineers, 2015.
[13] W. Qiu, J. Sales Junior, D. Lee, H. Lie, V. Magarovskii, T. Mikami, J.-M. Rousset, S. Sphaier, L. Tao, X. Wang, Uncertainties related to predictions of loads and responses for ocean and offshore structures, Ocean Engineering 86 (2014) 58–67. doi:10.1016/j.oceaneng.2014.02.031.
[14] ASME (ed.), Guide for Verification and Validation in Computational Solid Mechanics, Tech. Rep. ASME V&V 10-2006 (R2016) (2016).
[15] S. Vilsen, T. Sauder, A. J. Sørensen, Real-time hybrid model testing of moored floating structures using nonlinear finite element simulations, in: Dynamics of Coupled Structures, Vol. 4 of Conference Proceedings of the Society for Experimental Mechanics Series, Springer International Publishing, 2017, pp. 79–92.
[16] A. M. Rustad, C. M. Larsen, A. J. Sørensen, FEM modelling and automatic control for collision prevention of top tensioned risers, Marine Structures 21 (1) (2008) 80–112. doi:10.1016/j.marstruc.2007.04.003.
[17] D. Fergestad, S. A. Løtveit, Handbook on Design and Operations of Flexible Pipes, joint industry project "safe and cost effective operations of flexible pipes" Edition, 2015.
[18] N. Terkovics, S. A. Neild, M. Lowenberg, R. Szalai, B. Krauskopf, Substructurability: The effect of interface location on a real-time dynamic substructuring test, Proceedings of the Royal Society A: Mathematical, Physical and Engineering Science 472 (2192) (2016) 20160433. doi:10.1098/rspa.2016.0433.
[19] L. Zhang, G. Stepan, Exact stability chart of an elastic beam subjected to delayed feedback, Journal of Sound and Vibration 367 (2016) 219–232. doi:10.1016/j.jsv.2016.01.002.
[20] P. L. Drazin, S. Govindjee, K. M. Mosalam, Hybrid Simulation Theory for Continuous Beams, Journal of Engineering Mechanics 141 (7) (2015) 04015005. doi:10.1061/(ASCE)EM.1943-7889.0000909.
[21] D. Xiu, G. E. Karniadakis, Modeling uncertainty in flow simulations via generalized polynomial chaos, Journal of Computational Physics 187 (1) (2003) 137–167. doi:10.1016/S0021-9991(03)00092-5.
[22] I. M. Sobol, Sensitivity estimates for nonlinear mathematical models, Mathematical Modelling and Computational Experiments 1 (4) (1993) 407–414.
[23] B. Sudret, Global sensitivity analysis using polynomial chaos expansions, Reliability Engineering & System Safety 93 (7) (2008) 964–979. doi:10.1016/j.ress.2007.04.002.
[24] G. Blatman, B. Sudret, Adaptive sparse polynomial chaos expansion based on least angle regression, Journal of Computational Physics 230 (6) (2011) 2345–2367. doi:10.1016/j.jcp.2010.12.021.
[25] E. T. Jaynes, Information Theory and Statistical Mechanics, The Physical Review 106 (4) (1957) 620–630.
[26] G. Blatman, B. Sudret, An adaptive algorithm to build up sparse polynomial chaos expansions for stochastic finite element analysis, Probabilistic Engineering Mechanics 25 (2) (2010) 183–197. doi:10.1016/j.probengmech.2009.10.003.
[27] S. Marelli, B. Sudret, UQLAB : A framework for Uncertainty Quantification in MATLAB, SIAM Conference on Uncertainty Quantification (ICVRAM), USA, 2014, 2014.
[28] S. Marelli, B. Sudret, UQLab user manual – Polynomial chaos expansions, Tech. Rep. UQLab-V1.0-104, Chair of Risk, Safety & Uncertainty Quantification, ETH Zürich (2017).
[29] L. Le Gratiet, S. Marelli, B. Sudret, Metamodel-Based Sensitivity Analysis: Polynomial Chaos Expansions and Gaussian Processes, in: R. Ghanem, D. Higdon, H. Owhadi (Eds.), Handbook of Uncertainty Quantification, Springer International Publishing, Cham, 2015, pp. 1–37. doi:10.1007/978-3-319-11259-6_38-1.

AppendixA. Verification of `fixedFreeCableSegment`

As verification of the FE implementation, the eigenvalues and associated modeshapes computed from `fixedFreeCableStructure` are compared to a known analytical solution. We consider a polyester line, commonly used in mooring systems, whose nominal properties are given in Table 1. Its length is $L = 1934$ m and it is subjected to a vertical top tension of $T_0 = 2.5$ MN. Under the assumptions of infinite axial stiffness and zero submerged weight, its eigenfrequencies ω_i and associated modeshapes ϕ_i are given by:

$$\forall i \in \mathbb{N}^*, \omega_i = \frac{(2i-1)\pi}{2L}\sqrt{\frac{T_0}{m}} \text{ and } \phi_i(z) = (-1)^{i+1}\sin\left(\frac{(2i-1)\pi z}{2L}\right) \tag{A.1}$$

where m is the mass and added mass per unit of length, and ϕ_i is normalized so that $\phi_i(L) = 1$. The six first modeshapes obtained from this analytical solution are represented with solid lines in Fig. A.12, and the values of the 15 first eigenperiods are tabulated in the second column of Table A.3. These eigenmodes are compared to the results obtained for a `fixedFreeCableSegment` object with n_{el}=500 elements, whose axial stiffness has been increased by one order of magnitude (to mimic the infinite stiffness assumption used in the analytical model), and whose submerged weight has been set to zero. The eigenmodes of a `fixedFreeCableSegment` object are obtained numerically from the eigenvalue analysis of $M^{-1}K$, where M and K are obtained from the nonlinear static analysis. The corresponding eigenperiods are tabulated in the third column of Table A.3, and the difference with the analytical solution is found to be insignificant. When n_{el} is decreased to 80 elements (fourth column of Table A.3), the error is less than 1% for the 13 first modes, and the first modeshapes, compared in Fig. A.12a, also show excellent agreement. For higher modes, with eigenperiods less than 1.80 s, the model with n_{el}=80 becomes too coarse, with less than 12 elements per wavelength $4L/(2i-1)$, and the estimated eigenperiods become erroneous. So provided that n_{el} is chosen adequately, the dynamic system modelled by `fixedFreeCableSegment` can be considered as verified against the corresponding analytical solution.

In reality, several physical effects will make the eigenmodes of a a polyester line deviate from the ideal solution (A.1). (1) First, the elasticity of the polyester somewhat influences the dynamics of long lines. This is shown in the fifth column of Table A.3, in which eigenperiods are evaluated from a vertical `fixedFreeCableSegment`, now featuring its nominal stiffness. While the elasticity of the line does not influence significantly the ten first transverse modes, it must be accounted for when higher modes (with associated eigenperiods lower than 2.41s, in the present case) need to be modelled. (2) The submerged weight of the slender structure causes tension variations throughout the water column, which also affects the eigenmodes. By considering the the sixth column of Table A.3, it is seen that this effect has an impact on all modes, including the the lower modes, making the corresponding eigenperiods deviate by 2 to 3% from the previous solution. (3) Then, since such a polyester line is in general installed in an oblique way, it will exhibit static lateral deflections (of the order of 1% of the structure's length in the present case), due to its submerged weight. As shown in the sixth column of Table A.3, this change of static configuration has some effect on all eigenmodes. (4) Finally, the oblique line is subjected to the shear current introduced in the previous section. It is found to have an insignificant additional effect on the eigenmodes (last column in Table A.3). Note however that current has an important effect on the drag-induced damping of transverse motions.

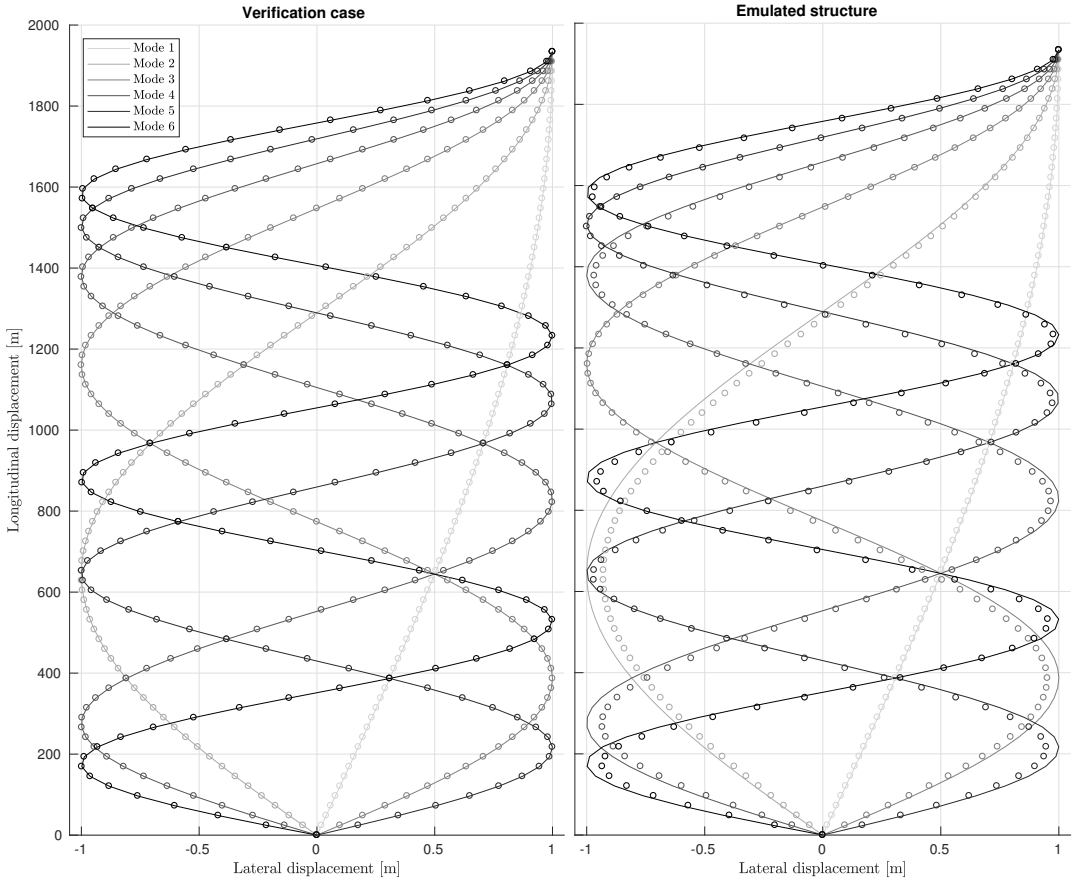

(a) Verification case: ideal cable.

(b) Modal analysis of the emulated structure with nominal weight in water, stiffness, and under inclined top force and current loads, and comparison with an ideal cable.

Figure A.12: Modeshapes corresponding to the six first eigenmodes of the fixed-free cable structure. Corresponding eigenperiods can be found in Table A.3. In both figures, the analytical solutions for an ideal (weightless and infinitely stiff) cable are plotted with solid lines, and numerical results using the `fixedFreeCableSegment` class with 80 elements are plotted with circle markers.

Table A.3: Eigenperiods in seconds corresponding to the 15 first modes of a 1934m long cable subjected to a top tension of 2.5MN. In italic: deviation in percents between the analytical solution (transverse vibrations of a weightless and infinitely stiff string) and various numerical solutions computed with the `fixedFreeCableSegment` class.

	Analytical solution	Numerical solution using the `fixedFreeCableSegment` class											
Axial stiffness	Infinite	Nominal × 10		Nominal × 10		Nominal		Nominal		Nominal		Nominal	
Weight in water	Weightless	Weightless		Weightless		Weightless		Nominal		Nominal		Nominal	
Top force direction	-	Vertical		Vertical		Vertical		Vertical		Nominal		Nominal	
Current	-	None		None		None		None		None		Nominal	
Number of elements	-	500	*%*	80	*%*	80	*%*	80	*%*	80	*%*	80	*%*
Mode 1	49.15	49.15	*0.00*	49.15	*0.00*	49.39	*0.48*	50.68	*3.12*	50.17	*2.08*	50.17	*2.07*
Mode 2	16.38	16.38	*0.00*	16.38	*-0.01*	16.46	*0.47*	16.78	*2.42*	16.66	*1.71*	16.66	*1.71*
Mode 3	9.83	9.83	*0.00*	9.83	*-0.04*	9.87	*0.44*	10.06	*2.33*	9.99	*1.62*	9.99	*1.62*
Mode 4	7.02	7.02	*0.00*	7.02	*-0.08*	7.05	*0.41*	7.18	*2.28*	7.13	*1.57*	7.13	*1.57*
Mode 5	5.46	5.46	*0.00*	5.45	*-0.13*	5.48	*0.35*	5.58	*2.22*	5.54	*1.51*	5.54	*1.51*
Mode 6	4.47	4.47	*0.00*	4.46	*-0.19*	4.48	*0.29*	4.56	*2.15*	4.53	*1.45*	4.53	*1.44*
Mode 7	3.78	3.78	*-0.01*	3.77	*-0.27*	3.79	*0.21*	3.86	*2.07*	3.83	*1.37*	3.83	*1.36*
Mode 8	3.28	3.28	*-0.01*	3.26	*-0.36*	3.28	*0.12*	3.34	*1.98*	3.32	*1.27*	3.32	*1.27*
Mode 9	2.89	2.89	*-0.01*	2.88	*-0.46*	2.89	*0.02*	2.95	*1.87*	2.92	*1.17*	2.92	*1.16*
Mode 10	2.59	2.59	*-0.01*	2.57	*-0.58*	2.58	*-0.10*	2.63	*1.76*	2.61	*1.05*	2.61	*1.05*
Mode 11	2.34	2.34	*-0.02*	2.32	*-0.70*	2.41	*2.92*	2.41	*2.90*	2.41	*2.88*	2.41	*2.87*
Mode 12	2.14	2.14	*-0.02*	2.12	*-0.84*	2.34	*9.28*	2.38	*11.30*	2.36	*10.53*	2.36	*10.53*
Mode 13	1.97	1.97	*-0.02*	1.95	*-0.99*	2.13	*8.30*	2.17	*10.31*	2.15	*9.54*	2.15	*9.54*
Mode 14	1.82	1.82	*-0.03*	1.80	*-1.16*	1.96	*7.44*	1.99	*9.43*	1.98	*8.67*	1.98	*8.67*
Mode 15	1.69	1.69	*-0.03*	1.67	*-1.34*	1.81	*6.67*	1.84	*8.65*	1.83	*7.90*	1.83	*7.89*

AppendixB. Convergence and parameter study for the co-simulation

We consider the taut polyester mooring line, truncated with α=0.8, and exposed to the current and wave-induced loads described in Section 2. The response of the substructured system is evaluated by the co-simulation procedure outlined previously. Each of the four parameters is varied, keeping the other ones constant and equal to the following nominal values: n_{el}=80 elements, δt=10 ms, ϵ_v=10^{-6} m/s and ϵ_f=0.1 N. As discussed in the previous section, the QoI for our problem are the top velocity of `p` and the bottom force of `n`. The following indicators are therefore used to study convergence:

$$\epsilon_1 = \left(\frac{\int_0^T \left(V_{x,top}(t) - V^{\infty}_{x,top}(t)\right)^2 dt}{\int_0^T V^{\infty}_{x,top}(t)^2 dt} + \frac{\int_0^T \left(V_{z,top}(t) - V^{\infty}_{z,top}(t)\right)^2 dt}{\int_0^T V^{\infty}_{z,top}(t)^2 dt} \right)^{1/2} \tag{B.1}$$

$$\epsilon_2 = \left(\frac{\int_0^T \left(F_{x,bottom}(t) - F^{\infty}_{x,bottom}(t)\right)^2 dt}{\int_0^T F^{\infty}_{x,bottom}(t)^2 dt} + \frac{\int_0^T \left(F_{z,bottom}(t) - F^{\infty}_{z,bottom}(t)\right)^2 dt}{\int_0^T F^{\infty}_{z,bottom}(t)^2 dt} \right)^{1/2} \tag{B.2}$$

where the $^{\infty}$ superscript refers to the time series obtained with the finest mesh, smallest synchronization time step or tolerance value, depending on which parameter is varied. Fig. B.13a to B.13d show the variations of ϵ_1 and ϵ_2 as a function of each parameter, and Fig. B.13e shows the effect of the parameters on the computational time.

As expected, ϵ_1 and ϵ_2 decrease when refining the mesh (Fig. B.13a), while the computational time increases proportionally to n_{el}^2 (Fig. B.13e). As seen in Section 4, the present study requires a possibly large number of co-simulations, n_{el}=80 is selected, which allows keeping computational costs to an acceptable level, with an ϵ_1 error of the order of 2%.

Convergence is also clearly observed when the synchronization time step is reduced (Fig. B.13b). It can be observed (Fig. B.13e) that the computational time is minimum for δt=10 ms, and increases significantly when δt=100ms. Indeed, even if reducing total number of synchronizations during the given simulation time, increasing δt leads to a larger required number of iterations (lines 6-14 in Alg. 1) at each synchronization step. On the other hand, it can be observed that the computational time is larger for δt=5ms than for δt=10ms. In that case, even if very few iterations are required to achieve compatibility and equilibrium, the total computational burden increases due to some expensive operations (such as writing data), which are performed at the end of each synchronization step.

Finally, as expected when considering line 11 in Alg. 1, ϵ_v and ϵ_f play a symmetric role. For a given ϵ_f for example, decreasing ϵ_v will only have an influence on the outcome of the co-simulation (and thus on ϵ_1 and ϵ_2) if it is ϵ_v, and not ϵ_f, that forces the iteration process to continue. Indeed, when ϵ_v is chosen to be very large, the dynamic equilibrium condition will be the limiting constraint, and the value of ϵ_f will thus steer the number of iterations. When ϵ_v is decreased and reaches a certain threshold, which depends on the mechanical impedance of the structure, it may be either the equilibrium or the compatibility condition that steers the number of iterations, at a given synchronization step. Finally, decreasing further ϵ_v will enforce an increased accuracy on the compatibility condition, which decreases the error, and increases the number of iterations and the computational time. This shift is clearly happening for ϵ_v=10^{-7} m/s in Fig. B.13c. It should however be noted, that within the range of investigated ϵ_v and ϵ_f, the errors ϵ_1 and ϵ_2 are extremely small.

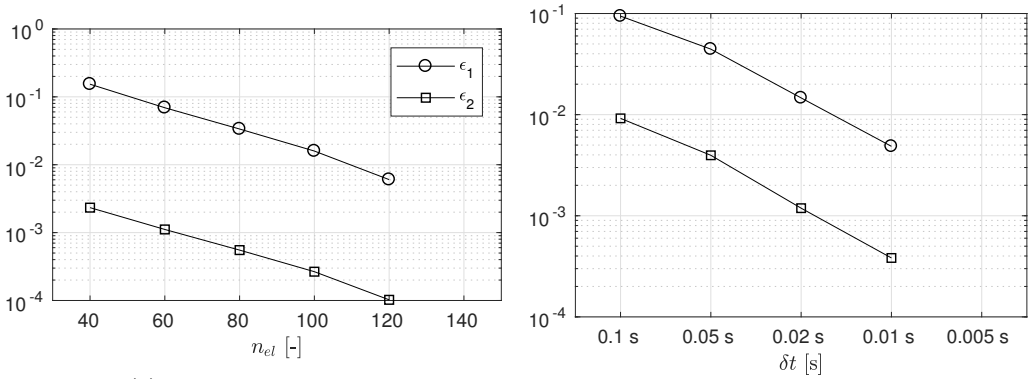

(a) Number of elements

(b) Time step

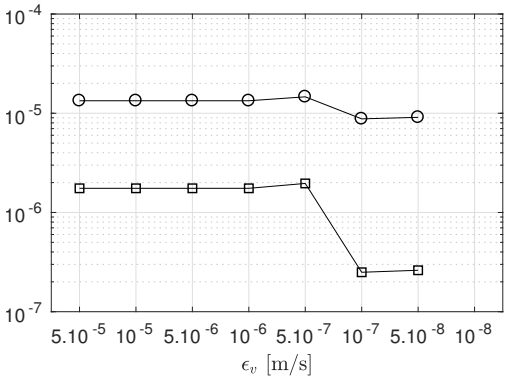

(c) Tolerance criterion - compatibility

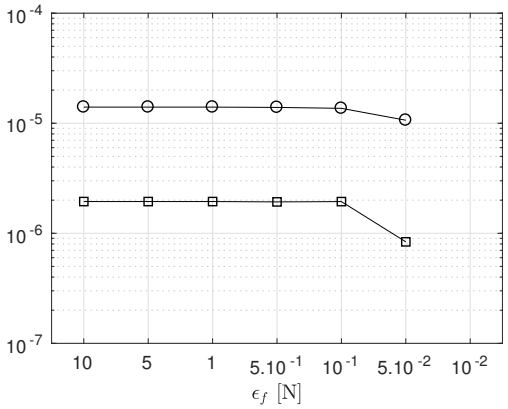

(d) Tolerance criterion - equilibrium

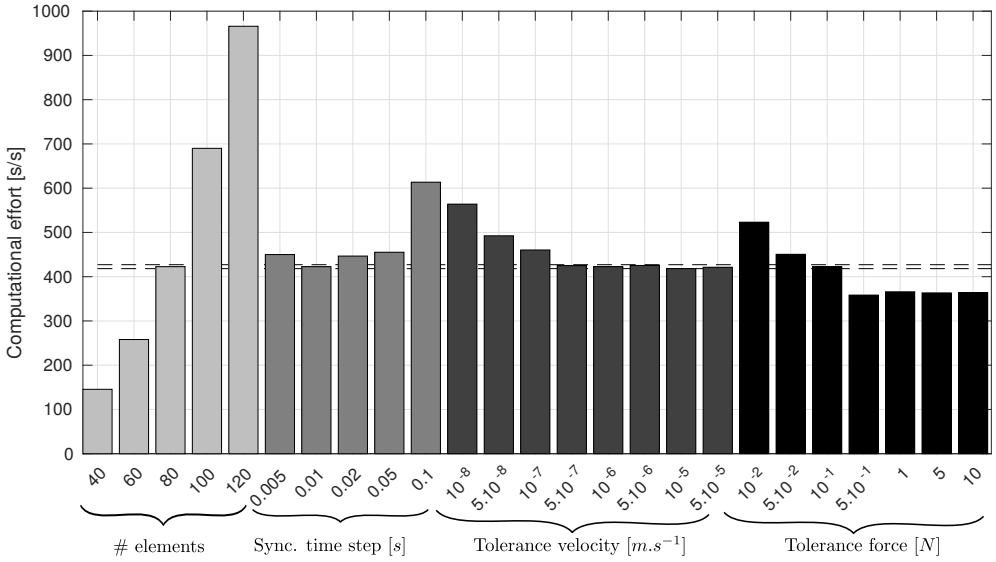

(e) Computational time: number of seconds required per simulated second. The dashed lines correspond to the mean value ± one standard deviation of the duration of the simulation using the nominal set of parameters.

Figure B.13: Convergence study. Effect of varying the number of elements, the synchronization time step and synchronization tolerances on the error indicators ε_1 and ε_2 (four top figures), and on the computational time (lower figure).